Intracellular Lactate Dynamics Reveal the Metabolic Diversity of *Drosophila* Glutamatergic Neurons

Matthew S. Price[1,2,3], Travis I. Moore[1,3], and Kartik Venkatachalam[1,2,3,4]

[1]Department of Integrative Biology and Pharmacology, McGovern Medical School at the University of Texas Health Sciences Center (UTHealth), Houston, TX, USA

[2]Neuroscience Graduate Program, The University of Texas MD Anderson Cancer Center UTHealth Houston Graduate School of Biomedical Sciences

[3]Molecular and Translational Biology Graduate Program, The University of Texas MD Anderson Cancer Center UTHealth Houston Graduate School of Biomedical Sciences

[4]Correspondence: kartik.venkatachalam@uth.tmc.edu

SUMMARY

Lactate, an intermediary between glycolysis and mitochondrial oxidative phosphorylation, reflects the metabolic state of neurons. Here, we utilized a genetically-encoded lactate FRET biosensor to uncover subpopulations of distinct metabolic states among *Drosophila* glutamatergic neurons. Neurons within specific subpopulations exhibited correlated lactate flux patterns that stemmed from inherent cellular properties rather than neuronal interconnectivity. Further, individual neurons exhibited consistent patterns of lactate flux over time such that stimulus-evoked changes in lactate were correlated with pre-treatment fluctuations. Leveraging these temporal autocorrelations, deep-learning models accurately predicted post-stimulus responses from pre-stimulus fluctuations. These findings point to the existence of distinct neuronal subpopulations, each characterized by unique lactate dynamics, and raise the possibility that neurons with correlated metabolic activities might synchronize across different neural circuits. Such synchronization, rooted in neuronal metabolic states, could influence information processing in the brain.

INTRODUCTION

Neurons are metabolically demanding cells[1]. The advent of genetically-encoded sensors of energy-related metabolites, such as ATP, glucose, pyruvate, lactate, and NAD^+/NADH, has revolutionized our understanding of the relationship between neuronal activity and bioenergetics[2]. These sensors have enabled elucidation of how neuronal activity affects ATP production, and have revealed mechanisms underlying the metabolic burden of neuronal excitability, Ca^{2+} extrusion, and synaptic transmission[1,3–7]. In addition, pioneering work in *Drosophila* has revealed strong correlations between activity and metabolism at the level of neuronal circuits[2,8]. These studies demonstrate that neurons allocate metabolic resources based on historical activity patterns, and that the metabolic states of interconnected neurons are correlated[8–11].

Cellular lactate production depends on the reduction of glycolysis-derived pyruvate by lactate dehydrogenase (LDH)[12,13]. In energetically demanding cells, such as neurons, lactate oxidation is a glucose-sparing source of pyruvate, which is taken up into the mitochondria to power the tricarboxylic acid (TCA) cycle and oxidative phosphorylation (OXPHOS)[14,15]. In both *Drosophila* and vertebrate brains, glia supply neurons with lactate as a substrate for energy production, especially during periods of heightened neuronal activity and computational load[15–19]. Oxidation of glia-derived lactate is necessary for the regulation of neuronal excitability, plasticity, and viability[15,17,19,20]. Indeed, application of lactate, rather than glucose, increases neuronal spiking activity in rodent cortical neurons[21]. Examinations of lactate flux can provide insights into the metabolic and redox states of neurons. For instance, preferential use of

lactate as a metabolic substrate reflects dependance on OXPHOS for energy production[21]. Since the cytosolic NAD^+/NADH ratio is a readout of the directionality of LDH activity (pyruvate-to-lactate versus lactate-to-pyruvate)[14,17], changes in [lactate] also reflect the redox balance of the cell[12]. In sum, lactate is a metabolite that stands at the crossroads of glycolysis, mitochondrial ATP production, and cellular redox state.

Our objective here was to understand how various metabolites and drugs that influence glycolysis and OXPHOS affect neuronal lactate dynamics at cellular resolution. Using the FRET-based lactate biosensor, Laconic[22], we found that treatments that affect metabolism induced significant changes in lactate flux in *Drosophila* glutamatergic neurons, albeit with notable cell-to-cell variability. Analysis at the population level revealed the existence of clusters of neurons that exhibited strongly correlated lactate flux dynamics, which argues that *Drosophila* glutamatergic neurons are comprised of subpopulations that differ in their metabolic states. The existence of response correlations among dissociated neurons also implied that correlations arose from cell intrinsic properties rather than from neuronal interconnectivity. Interestingly, treatment-induced patterns of lactate flux were correlated with steady-state, pre-treatment fluctuations in neuronal [lactate]. This allowed deep-learning models to accurately predict post-stimulus responses from pre-stimulus fluctuations in cytosolic [lactate]. Collectively, our results indicate that lactate flux is intricately linked to the metabolic state of neurons, and that the temporal dynamics of neuronal lactate flux are governed by cell-intrinsic properties that can be used to classify those cells into distinct metabolic subpopulations.

RESULTS

Drosophila glutamatergic neurons exhibit temporally correlated changes in cytosolic lactate in response to the application of glucose

Laconic[22] is a genetically-encoded, FRET-based lactate biosensor comprised of the lactate binding domain of the bacterial transcription factor, LldR, flanked by mTFP and Venus (Figure S1A). Proximity of the fluorophores in the absence of lactate binding (low [lactate]) results in constitutive mTFP–Venus FRET, which is abrogated when the sensor binds lactate (high [lactate])[22,23] (Figure S1A). Therefore, changes in cytosolic [lactate] are inversely related to mTFP–Venus FRET efficiency in cells expressing Laconic, which we refer to as the Laconic ratio[22,23]. Here, we expressed *UAS-Laconic*[24] under the control of the *d42-GAL4* glutamatergic/motor neuron driver[25,26] (*d42>Laconic*). Using confocal microscopy, we imaged live *d42>Laconic* neurons dissociated from the brains of 3rd instar larvae in an extracellular hemolymph-like buffer (HL3)[27], which contains trehalose (5 mM) and sucrose (115 mM), but no glucose (Figure 1A).

Given the purported importance of glucose to neuronal metabolism[28,29] and reports of glucose transporter (*Glut1*) expression in *Drosophila* neurons[30–33], we examined the changes in Laconic ratio in response to the application of HL3 containing glucose (5 mM final concentration). We found that the effects of glucose on neuronal Laconic ratios were highly variable (Figure 1B). This heterogeneity was reminiscent of the notion that the complexity and variability in the responses of individual neurons often obscure underlying patterns of organization at the population level[9,34]. Therefore, we reasoned

that the imaged neurons might be comprised of distinct subpopulations that exhibit intra-population similarities and inter-population differences in Laconic ratios[34].

To test this idea, we sought to uncover putative correlations in the population of Laconic ratios. We used dynamic time warping (DTW)[35] — an algorithm designed specifically for the assessment of correlations in time series data. DTW has the ability to handle nonlinear relationships between temporal segments and in sequences that are out of sync (i.e., vary in speed and phase). The algorithm also circumvents the restrictive nature of Euclidean time series matching by stretching or compressing segments to ensure optimal correlation (Figure 1C). Using DTW, we generated a distance matrix of the temporal correlations between the normalized Laconic ratios after glucose application. Ward's clustering[36], which seeks to minimize intra-cluster variance, revealed the presence of four clusters of correlated responses in glucose-treated cells (Figure 1D). Laconic ratios exhibited obvious intra-cluster similarities and inter-cluster differences (Figures 1E-1F). Examination of the integrated changes in ratio per unit time after application of glucose revealed that neurons belonging to cluster 1 exhibited a net decrease in Laconic ratio (i.e., increase in lactate binding), whereas neurons belonging to clusters 2-4 showed varying extents of ratio increase (Figure 1G). Together, these data point to the existence of distinct subgroups of neurons whose members exhibited correlated changes in lactate flux in response to glucose. Neurons that shared membership in a particular cluster were often neither plated on the same dish nor imaged on the same day. Many neurons with correlated changes in Laconic ratio did not even originate from the same animal. Therefore, the temporally correlated patterns of

lactate flux stemmed from inherent, cell autonomous properties of the imaged neurons rather than from interconnectivity in circuits.

Variances of Laconic ratios in the four clusters were between 5- and 20-fold lower than that of the full population of neurons (Figure 1H). To assess the statistical significance of these reductions in variance, we calculated the variance of shuffled sets of neurons sampled repeatedly from the full population. For the time points after the application of glucose, population variances of the shuffled responses were significantly higher than those in the corresponding clusters identified by DTW (Figure S1). Variances of Laconic ratios *prior* to the addition of glucose, however, were not significantly different between the real and shuffled clusters (Figure S1). These data indicate that inter-cluster variability appeared only after the application of glucose. In agreement, application of DTW and Ward's clustering on Laconic ratios from the period prior to the application of glucose revealed the presence of two relatively loose clusters whose overall responses to glucose were qualitatively similar (Figures 1I-1J and S1C). Therefore, correlated changes in lactate flux arose from the application of glucose.

Physical act of buffer application is sufficient to elicit correlated changes in lactate flux in dissociated *Drosophila* neurons

To determine the effects of the physical act of buffer application, we applied a sham control (HL3 without glucose, herein referred to as buffer application) and examined changes in cytosolic Laconic ratios. To our surprise, application of buffer alone was sufficient to elicit a plethora of changes in Laconic ratios (Figure 2A). DTW and

hierarchical clustering revealed the presence of three clusters of correlated response, each of which exhibited lower variance than that in the full set of neurons (Figures 2B-2C). Further, Laconic ratios in buffer-treated neurons exhibited intra-cluster similarities and inter-cluster differences (Figure 2D-2E). Together, these results demonstrate that the mere act of adding buffer to neurons was sufficient to elicit correlated changes in lactate flux in dissociated *Drosophila* glutamatergic neurons.

An autoencoder can effectively distinguish between the effects of glucose or buffer alone

We reasoned that glucose-induced changes in Laconic ratios reflected a composite of the responses to glucose and the physical act of buffer application. That we observed four clusters in response to glucose, while the buffer alone elicited only three clusters agreed with this logic. In our attempt to distinguish between responses that stemmed solely from buffer application and those that also reflected the effects of glucose, we were guided by the understanding that correlations in a population of neurons arise from shared low-dimensional statistical similarities. Because these underlying features are not directly evident from the higher-dimensional data, they are often referred to as being hidden or latent. The response of each neuron in a cluster is a different instantiation of a parsimonious latent response modified by individual noise. Importantly, examination of the latent characteristics of a cluster could reveal hidden statistical similarities and differences with other clusters.

These ideas led us to the autoencoder — an unsupervised deep-learning architecture that relies on uncovering the latent features of noisy input data[37–39]. Autoencoders are comprised of hidden encoder and latent layers that have progressively fewer nodes than the input layer[38] (Figure 3A). The progressive reduction in the number of nodes results in an informational bottleneck that forces the model to learn a compressed low-dimensional (i.e., latent) representation of the input data[37]. The decoder layers perform these operations in reverse, thereby reconstructing the original data from the latent representation[37,38]. The model is said to have learned an accurate latent representation that captures the nonlinear correlations in the input if the reconstructed data closely match the ground-truth. In the context of Laconic traces, we reasoned that if any two clusters have similar latent statistical structures, an autoencoder trained on one cluster would accurately reconstruct the other. Conversely, if the latent states of two clusters differ, the error associated with the reconstruction of the latter would be significantly higher. To test this idea, we generated a model comprised of an encoder with two hidden layers, a central latent layer, and a decoder with two hidden layers in an orientation that was opposite to that of the encoder (Figure 3A). We used the rectified linear unit (ReLU)[39] as the activation function in every layer except the last layer of the decoder, for which we used a linear function. We implemented dropout regularization to prevent complex coadaptation between the units during learning that can lead to overfitting[39,40].

When training on buffer cluster 1, this model accurately reconstructed the responses of this cluster (mean square error (MSE), 0.1353 ± 0.008; Figure 3B), which indicated

that the autoencoder can successfully learn the latent representation of a cluster of correlated Laconic ratios. MSE associated with reconstruction of glucose clusters 1 and 4 were significantly higher (2.822 ± 0.061 and 1.219 ± 0.103, respectively; Figure 3B), which argued that the latent representation of buffer cluster 1 was different from those of glucose clusters 1 and 4. In contrast, the model trained on buffer cluster 1 accurately reconstructed glucose cluster 2 (MSE, 0.1121 ± 0.009; Figure 3B). Because the MSE associated with reconstruction of glucose cluster 2 was statistically indistinguishable from that associated with reconstruction of buffer cluster 1 (Figure 3B), we conclude that these two clusters have similar latent representations. Although the reconstruction of glucose cluster 3 was ostensibly accurate, MSE associated with this reconstruction was still ~2-fold, and significantly, higher (0.2237 ± 0.023; Figure 3B).

We repeated this process by training the autoencoder on buffer clusters 2 and 3, and evaluating the reconstruction error associated with glucose clusters 1-4. By doing so, we generated a matrix of Bonferroni corrected *P*-values from pairwise comparisons of the MSE values (Figure 3C). This matrix revealed that buffer cluster 1 and glucose cluster 2 had similar latent representations. In agreement, normalized Laconic ratios associated with buffer cluster 1 and glucose cluster 2 overlapped almost perfectly (Figure 3D), while the other clusters exhibited distinct and non-overlapping ratios (Figure 3E). These data argue that the response of glucose cluster 2 predominantly reflected the effect of buffer application. In contrast, glucose modified the responses associated with buffer clusters 2 and 3, thus evoking three clusters of correlated Laconic ratios (glucose clusters 1, 3, and 4).

Responses of *Drosophila* glutamatergic neurons to the application of pyruvate and inhibitors of OXPHOS and glycolysis

To understand further the mechanisms of lactate regulation in fly glutamatergic neurons, we probed *d42>laconic* neurons for the effects of pyruvate application. We found that 1 mM pyruvate led to three clusters of correlated changes in the Laconic ratio (Figure 4A). Using the autoencoder trained on the responses to buffer alone, we found that buffer cluster 1 and pyruvate cluster 1 shared latent characteristics (Figure S2A). In agreement, Laconic traces of neurons belonging to these clusters overlapped (Figure 4B). Latent representations of buffer clusters 2 and 3 and pyruvate clusters 2 and 3, however, were different (Figure S2A). Laconic traces and integrated changes in Laconic ratios were clearly different between these clusters (Figures 4B-4C).

Next, we probed the effects of inhibiting complex V of the electron transport chain by the application of oligomycin A[41,42] (oligo A). 10 μM oligo A led to three clusters of correlated changes in the Laconic ratio (Figure 4D), of which clusters 1 and 2 shared latent characteristics with buffer clusters 1 and 2, respectively (Figures S2B and 4E). Latent representations of buffer cluster 3 and oligo A cluster 3 were distinct (Figures S2B and 4E). Application of the inhibitor of glycolysis, 2-deoxyglucose[43] (2DG, 10 mM final concentration), evoked two clusters of correlated Laconic responses (Figure 4G). The autoencoder revealed that 2DG cluster 1 shared latent structure with buffer cluster 3, leaving 2DG cluster 2 with a distinct latent state compared to buffer clusters 1 and 2 (Figures S2C and 4H-4I).

One-to-one comparisons of the integrated changes in Laconic ratios between clusters of correlated responses that share latent characteristics revealed that relative to application of buffer alone, application of pyruvate and oligo A resulted in significant net decrease and increase in [lactate], respectively (Figures 4C and 4F). In contrast, neither glucose nor 2DG evoked statistically significant changes in Laconic ratios relative to buffer alone (Figures 3D and 4I).

Assessment of the variability of Laconic responses in *Drosophila* glutamatergic neurons

Inclusion of metabolites (glucose or pyruvate) or drugs (oligo A or 2DG) in the recording buffer evoked correlated changes in neuronal lactate flux that were both similar and distinct from those brought about by the application of buffer alone. In the case of treatment-evoked subclasses whose latent characteristics were distinct from those evoked by the application of buffer alone, one-to-one comparisons of the integrated changes in Laconic ratios would not be meaningful. Therefore, we shifted our focus from examination of response averages to the assessment of *response variability*. This approach — motivated by information theory[44] — posits that greater response variability (i.e., higher entropy) indicates increases in system complexity and information content. The notion of information here refers to the ability of neurons to respond to stimuli in a more diverse set of ways, which suggests the engagement of novel metabolic pathways and/or alterations in the rates of lactate production and consumption.

Thus, we sought to characterize the variability in the range of Laconic responses within each cluster. Each cluster was comprised of different fractions of neurons that exhibited increases or decreases in [lactate] (e.g., magenta and green dots, respectively, Figure 5A). Using these cluster-specific distributions, we calculated the weighted probabilities for an increase or decrease in [lactate] (P_{pos} and P_{neg}, respectively), and used these probabilities to calculate the Shannon entropy[44] of that cluster (box, Figure 5A). Sum of the entropy values of all the clusters represented the overall entropy associated with a particular treatment. Upon comparing the ratios of entropies evoked by treatments relative to those evoked by buffer alone ($H_{treatement}/H_{buffer}$), we observed significant increases in entropies in response to glucose, pyruvate and oligo A (i.e., $H_{treatement}/H_{buffer} > 1$) (Figure 5B). For 2DG, P_{neg} for each cluster was zero, which prevented us from calculating entropies. Next, we calculated the ratios of entropies for each treatment after shuffling the cluster labels. The entropy ratios for the shuffled controls were significantly lower than those of the respective true ratios (Figure 5B). Therefore, application of glucose, pyruvate and oligo A, but not 2DG, elicited significant increases in information content (i.e., response variability) relative to application of buffer alone.

Evolution of low-dimensional projections of population responses

Based on previous studies[9,10,45], we reasoned that the underlying state of each cluster of neurons can be explained by covariance of a smaller number of latent variables. To identify these latent variables, we applied principal component analysis (PCA)[46] to reduce cluster dimensionality while preserving its variability. For each cluster, the first

three principal components (PC1, PC2, and PC3) captured >80% of the total variance associated with that cluster. By plotting the values of PC1, PC2, and PC3, we generated 3D representations of the latent states of the population (see Methods, Figures 6A-6D and S3A). In these phase plots, each point represents the state of all relevant neurons at a particular point in time. Evolution of the state over time (i.e., its temporal trajectory) is implicit, and was observed by color-coding the points on the basis of time (Figures 6A-6D and S3A).

We found that different clusters exhibited similarities and differences in their latent states' temporal trajectories. Monotonic changes in the trajectories were typically associated with low or zero entropy (e.g., buffer cluster 1, Figure 6A; glucose clusters 2 and 3, Figure 6B; pyruvate cluster 1, Figure 6C; and oligo A cluster 1, Figure 6D). In contrast, ring- or ball-shaped trajectories characterized the clusters with higher entropies (e.g., glucose cluster 4, Figure 6B; pyruvate cluster 3, Figure 6C; and oligo A cluster 3, Figure 6D). We also found that the shapes of the trajectories were similar between clusters that were determined by the autoencoder to share latent statistical features, and Laconic ratios associated with clusters of similarly shaped trajectories overlapped (Figure S3B). Together, these data indicate that clusters of neurons with similar changes in Laconic ratios share underlying latent states, and that the shape of the latent state trajectories are related to the information content of those clusters.

Fluctuations in Laconic ratios prior to treatment are predictive of the responses post-treatment

We asked whether the changes in neuronal [lactate] in response to the application of the buffer or a metabolite/drug correlated with the cells' preexisting metabolic states. If so, we should be able to predict the neurons' response categories from baseline fluctuations in Laconic ratios prior to treatment. To investigate this possibility, we trained a neural network[39] on z-scaled Laconic time series data from the pre-application period as input features, and the corresponding cluster identities as training labels (Figure 7A). Our model was comprised of a single hidden layer. We implemented dropout regularization and L1/L2 regularization in the hidden layer to mitigate the possibility of overfitting[39,40]. Using 5-fold cross-validation, we found that this model predicted cluster identities with accuracies ranging from ~60-90% (Figure 7B). Shuffling the training labels led to significant reductions in prediction accuracies (Figure 7B). In fact, prediction accuracies after label shuffling were no different from those expected by chance alone (i.e., by random guessing). The reductions in prediction accuracy after label shuffling indicate that the class labels were not inherently biased towards any particular outcome, and that the model learned meaningful patterns rather than noise and idiosyncrasies indicative of overfitting. Arguing further against overfitting, prediction accuracies for the training data was <5% higher than those for the test data (Figure 7C), which indicates that the model generalized well to unseen data. Together, these findings indicate that baseline fluctuations in neuronal [lactate] had inherent and detectable differences and similarities, even before the metabolites or drugs were added. Importantly, pre-treatment patterns in Laconic ratios correlated with the post-treatment response categories, which allowed our model to accurately classify a neuron's cluster identity from the pre-treatment Laconic ratios.

Next, we asked whether we can predict the post-treatment Laconic ratios from the pre-treatment time series data. We trained a neural network on z-scaled Laconic time series data from the pre-treatment period as input features, and the corresponding post-treatment scaled time series data as training labels (Figure 7D). This model was comprised of a single hidden layer. As in the previous case, we implemented dropout regularization and L1/L2 regularization in the hidden layer to mitigate overfitting[39]. Using 5-fold cross-validation, we found that the predicted Laconic responses closely matched the ground-truth (Figures 7E-7F). MSE associated with prediction were not significantly different for the training and test datasets (Figure 7G), which argues against overfitting. Training the model on scrambled post-response time-series led to the prediction of Laconic ratios that no longer matched the ground-truth (Figure 7F), and were therefore, characterized by significantly higher prediction error (Figure 7G). The only exception to this observation was the MSE associated with the prediction of oligo A-induced changes in Laconic ratios (Figure 7G). In this case, although the MSE associated with the scrambled dataset was higher than that associated with the ground-truth, these differences were not statistically significant after the application of the Bonferroni correction (Figure 7G). Based on these data, we conclude that with the exception of oligo A, our model accurately predicted post- treatment Laconic ratios directly from the pre- treatment values. These findings indicate that temporal dynamics of neuronal Laconic ratios pre- and post- treatment were correlated, and that our model was able to capture the details of these temporal autocorrelations.

DISCUSSION

Correlated lactate flux in dissociated glutamatergic neurons

Information processing in the brain stems from the coordinated activity of neuronal populations[9]. The collective behavior of a population of neurons is of greater significance to the processing of sensory inputs and determination of behavioral outputs than are the responses of individual neurons, an idea referred to as the "population doctrine"[9,45,47]. This doctrine frames a neuronal population as a coherent entity whose latent characteristics are related directly to the relevant sensory inputs or behavioral outputs[9,10,47]. In contrast, responses of single neurons are heterogenous, and their influence on sensation and behavior are harder to decipher. Our study of the changes in neuronal lactate flux — a proxy for the cells' metabolic state — agrees with this notion. Despite the heterogeneity in individual *Drosophila* neurons, we identified distinct subpopulations based on the correlated patterns of lactate flux. These data indicate that neurons labeled by the *d42-GAL4* glutamatergic/motor neuron driver are comprised of subpopulations of inherently distinct metabolic states. Future studies could be directed towards understanding whether these differences in metabolic states align with established motor neuron subtypes[48–50].

Contrary to the notion that synaptic interconnectivity is the driver of response correlation between neruons[8–11], our findings argue that the correlations in [lactate] arose from cell-intrinsic properties of neurons, independently of the constraints imposed by connectivity. This was evident in our observations of correlated responses among

neurons that were plated of separate dishes, dissociated from different animals, and imaged on different days. If these time-locked patterns of metabolic state evolution occur *in vivo*, it would be reasonable to assume their contribution to circuit-dependent response correlations in the brain. This idea agrees with recent reports of the preservation of neuronal population dynamics across different animals performing the same task despite idiosyncratic animal-to-animal differences in neuronal wiring[51]. In the event that unconnected circuits are comprised of neurons that exhibit correlations in cytosolic [lactate], simultaneous activation of those correlated neurons might impose inter-circuit synchronization. Insofar as rates of metabolite flux are coupled to neuronal activity[8], these modes of inter-circuit synchrony may be relevant to information processing.

Influence of external stimuli on neuronal lactate flux

Our findings highlight the sensitivity of neuronal lactate flux to external stimuli. Surprisingly, mere buffer application triggered significant changes in neuronal [lactate]. We speculate that mechanosensitive pathways may be responding to the changes in pressure and flow associated with buffer application and stimulating glycolysis, as has been reported in prior studies[52]. Mechanoresponsive Ca^{2+} channels, Inactive (Iav) and Piezo, are expressed and functional in *Drosophila* larval motor neurons[53–56]. Given that cytosolic [Ca^{2+}] elevations in neurons are sufficient for the stimulation of glycolysis[3], activation of Iav and Piezo during buffer application could induce glycolysis-dependent increase in [lactate].

According to the principle of thermodynamic additivity[57], two manipulations that induce additive increases in a cellular parameter are presumed to contribute to that parameter via independent (i.e., parallel) pathways. Conversely, non-additivity argues against response independence and suggests that the same downstream pathway is activated by either stimulus[57]. Seen through the lens of this principle, three lines of evidence suggest that the application of buffer led to the activation of glycolysis. First, additive increase in [lactate] upon inclusion of oligo A in the buffer indicates that the effects of buffer-alone occurred independently of mitochondria. Second, inclusion of glucose did not induce an additional increase [lactate], suggesting that buffer and glucose acted on the same downstream pathway — glycolysis. Third, buffer-induced increase in [lactate] in cluster 1 was abolished by inclusion of the glycolysis inhibitor, 2DG.

To differentiate the effects of buffer application from those induced by metabolites or drugs, we were guided by the understanding that correlated responses in a population arise from inherently shared statistical similarities. We trained an autoencoder to learn the compressed representation of the Laconic traces evoked by the application of buffer alone. By examining the accuracy with which this model predicted the response to metabolites and drugs, we identified clusters whose underlying statistical characteristics were the same as those evoked by buffer alone. Among these clusters, application of pyruvate led to a decrease in cytosolic [lactate]. These data point to pyruvate being sequestered into mitochondria to fuel the TCA cycle rather than being converted to lactate in the cytosol. The accompanying drop in [lactate] likely reflected the activity of

the malate-aspartate shuttle (MAS)[58], which maintains flux through the TCA cycle. By translocating electrons from the cytosol to mitochondria, MAS increases the cytosolic NAD^+/NADH ratio, which in turn forces LDH to oxidize cytosolic [lactate][58]. In support of the inverse relationship between mitochondrial activity and cytosolic [lactate], inhibition of OXPHOS by oligo A led to an increase in cytosolic [lactate].

In the case of clusters whose latent characteristics were significantly different from those evoked by buffer alone, we shifted our focus to Shannon entropy[44] — a measure of the neurons' ability to respond to stimuli in a more diverse set of ways. Relative to buffer alone, we observed increased response diversity to applications of glucose, pyruvate and oligo A. These data suggest that lactate flux, and by extension, neuronal activity[8], may be more diverse in response to metabolic stimuli. Such diversity might reflect alterations in neuronal states and influence neuronal activity.

Plots of the PCs agreed with the interpretations made permitted by the autoencoder. Clusters predicted by the autoencoder to share latent features exhibited similar phase state structures. This alignment between the actual phase states and those predicted by the autoencoder underscores the efficacy of the autoencoder in identifying underlying similarities among different clusters. Conversely, clusters predicted by the autoencoder to have distinct latent characteristics showed clear structural divergence in the phase plots. These data are consistent with our hypothesis of inherent metabolic state differences between the identified clusters. Another notable aspect of our analyses was the relationship between the overall entropy of a cluster and the shape of its latent state

trajectory. Steady, monotonic changes in trajectories, especially across PC1, defined clusters with low or zero entropy. Therefore, linear state space trajectories reflect a more predictable, uniform response pattern within these clusters of neurons. On the other hand, clusters with complex and non-linear trajectories, such as ring- or ball-shaped paths, were associated with higher entropies. These circular trajectories likely represent dynamic attractors in the system that influence neuronal responses to fluctuate around the baseline. In such clusters, [lactate] levels increased in some neurons and decreased in others, contributing to an overall elevation in Shannon entropy. This phenomenon indicates greater diversity of responses within these neuronal subpopulations.

Pre-stimulus fluctuations in cytosolic [lactate] are predictive of post-stimulus responses

Although pre-application fluctuations in cytosolic [lactate] were not correlated between neurons, we asked whether these fluctuations reflect the underlying metabolic state of the neurons, and thereby, influence the neurons' post-stimulus responses. Indeed, a deep-learning model could be trained to accurately predict post-application response categories from the pre-application time series. Since cluster identities were determined from correlations in Laconic ratios post-treatment, the pre-treatment Laconic ratios played no role in the assignment of response labels. Therefore, the accuracy of our model implies that pre-treatment fluctuations in [lactate] — equivalent to the baseline metabolic state of the neurons — correlated strongly with post-treatment responses. Our findings also indicate that whether a particular neuron sorted to one cluster or

another was not simply a stochastic outcome of buffer application. Instead, post-application responses were predetermined by their initial metabolic states. Further reinforcing this idea, we developed another model that predicted actual post-treatment Laconic traces from pre-treatment data. The impressive predictive accuracy of this model suggests autocorrelation between pre- and post-application lactate dynamics, which aligns with the concept that neurons' spontaneous activity patterns may act as foundational elements for top-down predictive models in the brain[59]. In sum, these findings demonstrate that the seemingly random fluctuations in neuronal [lactate] prior to treatment carried critical information that prefigured the neuron's metabolic response to a stimulus.

Limitations of the study and future directions

Alterations in cytosolic [lactate] that we describe in this study occurred in neurons dissociated from the brains of 3rd instar larvae. Dissociation of brains was needed to ensure that the applied metabolites or drugs had direct access to neurons without having to traverse the glial blood brain barrier. It is possible that changes in neuronal [lactate] might be qualitatively different in the intact brain where neurons receive trophic support from glia[16,17]. To overcome this limitation in future studies, we hope to examine neuronal [lactate] in intact brains, and the relationship between this metabolite and neuronal activity. For the latter, we would determine the effects of optogenetic stimulation/inhibition of neurons on cytosolic lactate flux. These studies would nicely complement prior work focused on the relationships between activity and the levels of pyruvate and ATP in brains of live flies[8].

Although our studies have revealed the existence of *d42-GAL4*-labeled neurons that exhibit correlated changes in lactate flux, whether these neurons constitute transcriptionally-defined subpopulations remains to be assessed. A variation of Patch-Seq[60], whereby RNA from imaged neurons is extracted and sequenced by single cell RNA-seq (scRNA-seq), could be a potential strategy to assess whether neurons exhibiting correlated responses belong to transcriptionally-defined subtypes. By generating *GAL4* drivers using the markers identified by scRNA-seq, we could determine the locations of these neurons in the brain and the types of circuits into which they integrate. Further, these subtype-specific markers reveal markers would allow us track neurons that exhibit correlated changes in lactate flux, thereby allowing us to ask whether they exhibit correlated changes in other metabolic parameters such [glucose], [pyruvate], ATP/ADP ratio, and NAD^+/NADH ratio using optical sensors[2].

ACKNOWLEDGEMENTS

We thank the Bloomington *Drosophila* Stock Center for fly stocks and Dr. Gregory Macleod for the *UAS-Laconic* fly line[24]. Live-cell fluorescence microscopy and image analysis was performed at the Center for Advanced Microscopy, a Nikon Center of Excellence, in the Department of Integrative Biology & Pharmacology at McGovern Medical School, UTHealth Houston (UTHealth). We are grateful to Aditya Singh for his invaluable suggestions regarding the use of machine learning algorithms, and Drs. Elham Rastegari and Richa Gupta for helpful discussions. This work was supported by National Institutes of Health (NIH) grants K01HL143111 to T.I.M, and RF1AG069076 and RF1AG072176 to K.V.

AUTHOR CONTRIBUTIONS

M.S.P., T.I.M. and K.V. designed the research; M.S.P. performed all the experiments with assistance from T.I.M. and K.V.; M.S.P. and K.V. analyzed data and wrote the manuscript.

DECLARATION OF INTERESTS

The authors declare no competing interests.

Methods

Resource Availability

Lead contact

Further information and requests for resources and reagents should be directed to and will be fulfilled by the lead contact, Dr. Kartik Venkatachalam (kartik.venkatachalam@uth.tmc.edu).

Materials availability

This study did not generate new unique reagents.

Data and code availability

1. All data reported in this paper will be shared by the lead contact upon request.
2. All original analysis code has been deposited and made publicly available (https://github.com/kvenkatachalam-lab/Price-et-al-2024).
3. Any additional information required to reanalyze the data reported in this paper is available from the lead contact upon request.

Method Details

Drosophila husbandry

All flies were reared at 21°C on standard fly food (per 1L of food: 95 g agar, 275 g Brewer's yeast, 520 g cornmeal, 110 g sugar, 45 g propionic acid, and 36 g Tegosept). We obtained the *d42-GAL4*, a driver fly line for transgene expression motor

neurons[25,26], from Bloomington *Drosophila* Stock Center, and the *UAS-Laconic*[24] transgenic line from the laboratory of Dr. Gregory Macleod.

Dissociation of *Drosophila* neurons

We dissociated neurons from *Drosophila* larval brains as described previously[7,61]. Briefly, we sterilized wandering 3rd instar *d42>Laconic* larvae by immersion in ethanol, followed by a wash in sterile water. We dissected brains from these larvae in primary neuron culture media comprised of Schneider's insect medium (S0146; Sigma-Aldrich) supplemented with 10% fetal bovine serum (FBS), antibiotic/antimycotic solution (A5955; Sigma-Aldrich), and 50 mg/ml of insulin (I6634; Sigma-Aldrich). After dissection, we washed the brains using fresh primary neuron culture media and then transferred the brains to a dissociation solution comprised of filter-sterilized HL-3 (70 mM NaCl, 5 mM KCl, 1 mM $CaCl_2$, 20 mM $MgCl_2$, 10 mM $NaHCO_3$, 115 mM sucrose, 5 mM trehalose, and 5 mM HEPES) supplemented with 0.4 mM L-cysteine (2430; Calbiochem), and 5 U/ml papain (P4762; Sigma-Aldrich). Larval brains were then placed in an incubator at 25°C for 30 minutes to be enzymatically digested by the papain solution. Following a wash in primary neuron culture media, we transferred papain-treated brains to a 1.5-ml tube containing 150 µl of primary neuron culture media, and dissociated them by trituration. We then plated the dissociated neurons on 35-mm glass bottom dishes (D35-10-0-N; Cellvis) pretreated with concanavalin-A (C2010; Sigma-Aldrich). Cells were thereafter stored in a humidified container for four days in primary neuron culture media in a 25°C incubator. We washed the preparations

with PBS once daily to eliminate any debris that may have remained from dissociation and to remove any yeast contamination.

Confocal imaging of dissociated *Drosophila* neurons

Confocal imaging of dissociated neurons was performed in accordance with previously-described methods[7,22,24,61]. Briefly, we used a Nikon A1R laser-scanning confocal for live-cell imaging on a Nikon TI-E inverted microscope equipped with Nikon 40x/1.3 NA Plan-Fluor oil immersion objective and the Perfect Focus System for maintenance of focus over time to excite Laconic with the 445 nm laser line and emission signals recorded at 488 nm (mTFP) and 535 nm (Venus). Immediately prior to imaging, primary neuron culture media was aspirated from plates of dissociated neurons and replaced with 50 µl of HL-3 at room temperature. We recorded baseline signals for 2-minutes prior to the application of 50 µl of HL-3 (buffer alone) or 50 µl of HL-3 containing metabolites or drugs at twice the final concentrations. We imaged ~20 cells per field, and conducted at least 3 biological replicates for each treatment over the course of multiple days.

Calculation of Laconic ratios and integrated changes in ratio in response to treatments

For each cover slip, we obtained fluorescence emissions at 488 nm (mTFP) and 535 nm (Venus) from regions of interest (ROI) corresponding to individual neuronal cell bodies. To correct for background, we subtracted the intensities of an ROI lacking cells from the intensities of the neuronal ROIs. Next, we calculated the ratio of background-

corrected emission intensities (mTFP/Venus) and normalized these ratios to the means of their corresponding baseline values. We determined the integrated changes in normalized Laconic ratios by calculating the area under the curve (AUC) for each trace from the time of treatment to the end of the recording. We used the CausalImpact package[62] in R to extrapolate the baseline to the end of the recording, and thereby, estimated the Laconic ratio had we not applied the treatment. Difference between the AUC value of a trace and that of its extrapolated baseline, adjusted for the length of time after the treatment, represented the integrated change in Laconic ratio.

DTW (Dynamic Time Warping) and time series clustering

Using the R packages for calculating proximity measures, proxy (available at https://cran.r-project.org/web/packages/proxy/index.html), and for DTW, dtw[63], we generated DTW distance matrix from Laconic ratio time series data. We generated dendrograms from the DTW distance matrices using Ward's agglomerative clustering method[36], and determined the number of clusters on the basis of maximal silhouette width derived by partitioning the cophenetic distance matrix of the dendrogram around medoids (find_k function in the R package, dendextend[64]).

Design of the autoencoder

Using the R packages for keras and TensorFlow[65] (https://tensorflow.rstudio.com), we generated an autoencoder comprised of an encoder with two hidden layers of 40 and 30 nodes, a central latent layer of 20 units, and a decoder with two hidden layers of 30 and 40 nodes. We used the rectified linear unit (ReLU)[39] as the activation function in every

layer except the last layer of the decoder, for which we used a linear function. We implemented dropout regularization (rate=0.2) to mitigate overfitting[39,40].

Calculation of Shannon's entropy

To assess the variability in response to a treatment, we used Shannon's entropy, a measure of uncertainty or unpredictability[44]. To calculate the Shannon's entropy for each cluster linked with a treatment, we first calculated the likelihood (weighted probabilities) of observing an increase or decrease in integrated change in Laconic ratio (refer to Figure 5A). We then computed the Shannon's entropy using the formula,

$$H_{cluster} = -P_{pos}\log_2 P_{pos} - P_{neg}\log_2 P_{neg}$$

In this formula, P_{pos} and P_{neg} represent the weighted probabilities of increase or decrease in integrated change in Laconic ratio, respectively. The total entropy for a treatment was obtained by summing the entropies of all the associated clusters. To evaluate the likelihood of these entropy changes occurring by chance, we performed bootstrap tests. This involved randomly scrambling the labels associated with the integrated changes in Laconic ratio for both the treatment and the control (buffer-only) conditions. After scrambling, we recalculated the relative change in entropy. This process was repeated 1000 times to create a 'null' dataset, which was then compared against the actual change in entropy linked to that treatment.

Generation of 3D representations of the latent states

We used scaled Laconic ratios for all the neurons associated with a cluster for the generation of 3D representations of that cluster's latent state. Briefly, we performed

PCA 1000 times on randomly sampled subsets of the data (30% of cells were considered in each run). This resampling approach aimed to ensure that we generated a robust and generalizable representation of the data's structure that also minimized the impact of outliers and noise. We plotted the resulting PCs and color coded the individual points on the basis of the time with which they were associated.

Neural network to predict patterns of changes in Laconic ratios

To predict the neurons' response categories from baseline fluctuations in Laconic ratios prior to treatment, we trained a neural network on z-scaled Laconic time series data. The training model was comprised of a single hidden layer of 32 units with ReLU activation function. Units of the output layer used the SoftMax activation function[39]. We implemented dropout regularization (rate=0.5) and L1/L2 regularization (rates=0.001) in the hidden layer to mitigate overfitting[39,40]. We used 5-fold cross-validation to predict cluster identities. To evaluate the likelihood of these prediction accuracies occurring by chance, we performed bootstrap tests. This involved randomly scrambling the response labels associated with each trace. After scrambling, we recalculated accuracy of prediction. This process was repeated 300 times to create a 'null' dataset, which was then compared against the actual prediction accuracy.

To determine whether we can predict the post-application Laconic ratios from the pre-application time series data, we trained another neural network on z-scaled Laconic time series data from the pre-application period as input features, and the corresponding post-application scaled time series data as training labels. This model

was comprised of a single hidden layer of 50 units. Both this and the output layer used linear activation functions. We implemented dropout regularization (rate=0.2) and L1/L2 regularization (rates=0.01) in the hidden layer to mitigate overfitting[39]. We determined prediction accuracies from 5-fold cross-validation using MSE as the metric of accuracy.

REFERENCES

1. Yellen, G. (2018). Fueling thought: Management of glycolysis and oxidative phosphorylation in neuronal metabolism. Journal of Cell Biology *217*, 2235–2246. 10.1083/jcb.201803152.
2. Barros, L.F., Ruminot, I., Sandoval, P.Y., and San Martín, A. (2023). Enlightening brain energy metabolism. Neurobiol Dis *184*, 106211. 10.1016/J.NBD.2023.106211.
3. Díaz-García, C.M., Mongeon, R., Lahmann, C., Koveal, D., Zucker, H., and Yellen, G. (2017). Neuronal Stimulation Triggers Neuronal Glycolysis and Not Lactate Uptake. Cell Metab *26*, 361-374.e4. 10.1016/j.cmet.2017.06.021.
4. Díaz-García, C.M., Meyer, D.J., Nathwani, N., Rahman, M., Martínez-François, J.R., and Yellen, G. (2021). The distinct roles of calcium in rapid control of neuronal glycolysis and the tricarboxylic acid cycle. Elife *10*. 10.7554/eLife.64821.
5. Ashrafi, G., Wu, Z., Farrell, R.J., and Ryan, T.A. (2017). GLUT4 Mobilization Supports Energetic Demands of Active Synapses. Neuron *93*, 606-615.e3. 10.1016/j.neuron.2016.12.020.
6. Rangaraju, V., Calloway, N., and Ryan, T.A. (2014). Activity-Driven Local ATP Synthesis Is Required for Synaptic Function. Cell *156*, 825–835. 10.1016/j.cell.2013.12.042.
7. Karagas, N.E., Gupta, R., Rastegari, E., Tan, K.L., Leung, H.H., Bellen, H.J., Venkatachalam, K., and Wong, C.-O. (2022). Loss of Activity-Induced Mitochondrial ATP Production Underlies the Synaptic Defects in a *Drosophila*

Model of ALS. The Journal of Neuroscience, JN-RM-2456-21. 10.1523/JNEUROSCI.2456-21.2022.

8. Mann, K., Deny, S., Ganguli, S., and Clandinin, T.R. (2021). Coupling of activity, metabolism and behaviour across the Drosophila brain. Nature *593*, 244–248. 10.1038/s41586-021-03497-0.

9. Cunningham, J.P., and Yu, B.M. (2014). Dimensionality reduction for large-scale neural recordings. Nat Neurosci *17*, 1500–1509. 10.1038/nn.3776.

10. Gallego, J.A., Perich, M.G., Miller, L.E., and Solla, S.A. (2017). Neural Manifolds for the Control of Movement. Neuron *94*, 978–984. 10.1016/j.neuron.2017.05.025.

11. Tsodyks, M., Kenet, T., Grinvald, A., and Arieli, A. (1999). Linking Spontaneous Activity of Single Cortical Neurons and the Underlying Functional Architecture. Science (1979) *286*, 1943–1946. 10.1126/science.286.5446.1943.

12. Li, H., Rai, M., Buddika, K., Sterrett, M.C., Luhur, A., Mahmoudzadeh, N.H., Julick, C.R., Pletcher, R.C., Chawla, G., Gosney, C.J., et al. (2019). Lactate dehydrogenase and glycerol-3-phosphate dehydrogenase cooperatively regulate growth and carbohydrate metabolism during Drosophila melanogaster larval development. Development *146*. 10.1242/dev.175315.

13. Vander Heiden, M.G., Cantley, L.C., and Thompson, C.B. (2009). Understanding the Warburg effect: the metabolic requirements of cell proliferation. Science *324*, 1029–1033. 10.1126/science.1160809.

14. Dienel, G.A. (2012). Brain lactate metabolism: the discoveries and the controversies. J Cereb Blood Flow Metab *32*, 1107–1138. 10.1038/jcbfm.2011.175.

15. Cauli, B., Dusart, I., and Li, D. (2023). Lactate as a determinant of neuronal excitability, neuroenergetics and beyond. Neurobiol Dis *184*, 106207. 10.1016/J.NBD.2023.106207.

16. González-Gutiérrez, A., Ibacache, A., Esparza, A., Barros, L.F., and Sierralta, J. (2020). Neuronal lactate levels depend on glia-derived lactate during high brain activity in Drosophila. Glia *68*, 1213–1227. 10.1002/glia.23772.

17. Magistretti, P.J., and Allaman, I. (2018). Lactate in the brain: from metabolic end-product to signalling molecule. Nat Rev Neurosci *19*, 235–249. 10.1038/nrn.2018.19.

18. Dembitskaya, Y., Piette, C., Perez, S., Berry, H., Magistretti, P.J., and Venance, L. (2022). Lactate supply overtakes glucose when neural computational and cognitive loads scale up. Proceedings of the National Academy of Sciences *119*, e2212004119. 10.1073/pnas.2212004119.

19. Volkenhoff, A., Weiler, A., Letzel, M., Stehling, M., Klämbt, C., and Schirmeier, S. (2015). Glial Glycolysis Is Essential for Neuronal Survival in Drosophila. Cell Metab *22*, 437–447. 10.1016/j.cmet.2015.07.006.

20. Long, D.M., Frame, A.K., Reardon, P.N., Cumming, R.C., Hendrix, D.A., Kretzschmar, D., and Giebultowicz, J.M. (2020). Lactate dehydrogenase expression modulates longevity and neurodegeneration in Drosophila melanogaster. Aging *12*, 10041–10058. 10.18632/aging.103373.

21. Karagiannis, A., Gallopin, T., Lacroix, A., Plaisier, F., Piquet, J., Geoffroy, H., Hepp, R., Naudé, J., Le Gac, B., Egger, R., et al. (2021). Lactate is an energy

substrate for rodent cortical neurons and enhances their firing activity. Elife *10*. 10.7554/eLife.71424.

22. San Martín, A., Ceballo, S., Ruminot, I., Lerchundi, R., Frommer, W.B., and Barros, L.F. (2013). A genetically encoded FRET lactate sensor and its use to detect the Warburg effect in single cancer cells. PLoS One *8*, e57712. 10.1371/journal.pone.0057712.
23. Baeza-Lehnert, F., Flores, C.A., Guequén, A., and Barros, L.F. (2020). Monitoring Lactate Dynamics in Individual Macrophages with a Genetically Encoded Probe. In (Humana, New York, NY), pp. 19–30. 10.1007/978-1-0716-0802-9_2.
24. Justs, K.A., Sempertegui, S., Riboul, D. V., Oliva, C.D., Durbin, R.J., Crill, S., Stawarski, M., Su, C., Renden, R.B., Fily, Y., et al. (2023). Mitochondrial phosphagen kinases support the volatile power demands of motor nerve terminals. J Physiol *601*, 5705–5732. 10.1113/JP284872.
25. Brand, A.H., and Perrimon, N. (1993). Targeted gene expression as a means of altering cell fates and generating dominant phenotypes. Development *118*, 401–415.
26. Parkes, T.L., Elia, A.J., Dickinson, D., Hilliker, A.J., Phillips, J.P., and Boulianne, G.L. (1998). Extension of Drosophila lifespan by overexpression of human SOD1 in motorneurons. Nat Genet *19*, 171–174. 10.1038/534.
27. Stewart, B.A., Atwood, H.L., Renger, J.J., Wang, J., and Wu, C.F. (1994). Improved stability of Drosophila larval neuromuscular preparations in haemolymph-like physiological solutions. J Comp Physiol A *175*, 179–191. 10.1007/bf00215114.

28. Lundgaard, I., Li, B., Xie, L., Kang, H., Sanggaard, S., Haswell, J.D.R., Sun, W., Goldman, S., Blekot, S., Nielsen, M., et al. (2015). Direct neuronal glucose uptake heralds activity-dependent increases in cerebral metabolism. Nat Commun *6*, 6807. 10.1038/ncomms7807.

29. Li, H., Guglielmetti, C., Sei, Y.J., Zilberter, M., Le Page, L.M., Shields, L., Yang, J., Nguyen, K., Tiret, B., Gao, X., et al. (2023). Neurons require glucose uptake and glycolysis in vivo. Cell Rep *42*, 112335. 10.1016/j.celrep.2023.112335.

30. Volkenhoff, A., Hirrlinger, J., Kappel, J.M., Klämbt, C., and Schirmeier, S. (2018). Live imaging using a FRET glucose sensor reveals glucose delivery to all cell types in the Drosophila brain. J Insect Physiol *106*, 55–64. 10.1016/J.JINSPHYS.2017.07.010.

31. Musso, P.-Y., Junca, P., and Gordon, M.D. (2021). A neural circuit linking two sugar sensors regulates satiety-dependent fructose drive in Drosophila. Sci Adv *7*, eabj0186. 10.1126/sciadv.abj0186.

32. Oh, Y., Lai, J.S.-Y., Mills, H.J., Erdjument-Bromage, H., Giammarinaro, B., Saadipour, K., Wang, J.G., Abu, F., Neubert, T.A., and Suh, G.S.B. (2019). A glucose-sensing neuron pair regulates insulin and glucagon in Drosophila. Nature *574*, 559–564. 10.1038/s41586-019-1675-4.

33. de Tredern, E., Rabah, Y., Pasquer, L., Minatchy, J., Plaçais, P.-Y., and Preat, T. (2021). Glial glucose fuels the neuronal pentose phosphate pathway for long-term memory. Cell Rep *36*, 109620. 10.1016/j.celrep.2021.109620.

34. Okun, M., Steinmetz, N.A., Cossell, L., Iacaruso, M.F., Ko, H., Barthó, P., Moore, T., Hofer, S.B., Mrsic-Flogel, T.D., Carandini, M., et al. (2015). Diverse coupling of

neurons to populations in sensory cortex. Nature *521*, 511–515. 10.1038/nature14273.

35. Berndt, D., and Clifford, J. (1994). Using Dynamic Time Warping to Find Patterns in Time Series. KDD Workshop.

36. Murtagh, F., and Legendre, P. (2014). Ward's Hierarchical Agglomerative Clustering Method: Which Algorithms Implement Ward's Criterion? J Classif *31*, 274–295. 10.1007/s00357-014-9161-z.

37. Kriegeskorte, N. (2015). Deep Neural Networks: A New Framework for Modeling Biological Vision and Brain Information Processing. Annu Rev Vis Sci *1*, 417–446. 10.1146/annurev-vision-082114-035447.

38. Hinton, G.E., and Salakhutdinov, R.R. (2006). Reducing the Dimensionality of Data with Neural Networks. Science (1979) *313*, 504–507. 10.1126/science.1127647.

39. LeCun, Y., Bengio, Y., and Hinton, G. (2015). Deep learning. Nature *521*, 436–444. 10.1038/nature14539.

40. Hinton, G.E., Srivastava, N., Krizhevsky, A., Sutskever, I., and Salakhutdinov, R.R. (2012). Improving neural networks by preventing co-adaptation of feature detectors.

41. RACKER, E. (1963). A mitochondrial factor conferring oligomycin sensitivity on soluble mitochondrial ATPase. Biochem Biophys Res Commun *10*, 435–439. 10.1016/0006-291x(63)90375-9.

42. LARDY, H.A., JOHNSON, D., and McMURRAY, W.C. (1958). Antibiotics as tools for metabolic studies. I. A survey of toxic antibiotics in respiratory, phosphorylative

and glycolytic systems. Arch Biochem Biophys *78*, 587–597. 10.1016/0003-9861(58)90383-7.

43. WICK, A.N., DRURY, D.R., NAKADA, H.I., and WOLFE, J.B. (1957). Localization of the primary metabolic block produced by 2-deoxyglucose. J Biol Chem *224*, 963–969.

44. Shannon, C.E. (1948). A Mathematical Theory of Communication. Bell System Technical Journal *27*, 379–423. 10.1002/j.1538-7305.1948.tb01338.x.

45. Ebitz, R.B., and Hayden, B.Y. (2021). The population doctrine in cognitive neuroscience. Neuron *109*, 3055–3068. 10.1016/j.neuron.2021.07.011.

46. Principal Component Analysis for Special Types of Data (2002). In Principal Component Analysis (Springer-Verlag), pp. 338–372. 10.1007/0-387-22440-8_13.

47. Saxena, S., and Cunningham, J.P. (2019). Towards the neural population doctrine. Curr Opin Neurobiol *55*, 103–111. 10.1016/J.CONB.2019.02.002.

48. Davie, K., Janssens, J., Koldere, D., De Waegeneer, M., Pech, U., Kreft, Ł., Aibar, S., Makhzami, S., Christiaens, V., Bravo González-Blas, C., et al. (2018). A Single-Cell Transcriptome Atlas of the Aging Drosophila Brain. Cell *174*, 982-998.e20. 10.1016/j.cell.2018.05.057.

49. Pérez-Moreno, J.J., and O'Kane, C.J. (2019). GAL4 Drivers Specific for Type Ib and Type Is Motor Neurons in Drosophila. G3 (Bethesda) *9*, 453–462. 10.1534/g3.118.200809.

50. Enriquez, J., Venkatasubramanian, L., Baek, M., Peterson, M., Aghayeva, U., and Mann, R.S. (2015). Specification of individual adult motor neuron morphologies by

combinatorial transcription factor codes. Neuron *86*, 955–970. 10.1016/j.neuron.2015.04.011.

51. Safaie, M., Chang, J.C., Park, J., Miller, L.E., Dudman, J.T., Perich, M.G., and Gallego, J.A. (2023). Preserved neural dynamics across animals performing similar behaviour. Nature *623*, 765–771. 10.1038/s41586-023-06714-0.

52. Park, J.S., Burckhardt, C.J., Lazcano, R., Solis, L.M., Isogai, T., Li, L., Chen, C.S., Gao, B., Minna, J.D., Bachoo, R., et al. (2020). Mechanical regulation of glycolysis via cytoskeleton architecture. Nature *578*, 621–626. 10.1038/s41586-020-1998-1.

53. Gong, Z. (2004). Two Interdependent TRPV Channel Subunits, Inactive and Nanchung, Mediate Hearing in Drosophila. Journal of Neuroscience *24*, 9059–9066. 10.1523/JNEUROSCI.1645-04.2004.

54. Wong, C.-O., Chen, K., Lin, Y.Q., Chao, Y., Duraine, L., Lu, Z., Yoon, W.H., Sullivan, J.M., Broadhead, G.T., Sumner, C.J., et al. (2014). A TRPV channel in Drosophila motor neurons regulates presynaptic resting Ca2+ levels, synapse growth, and synaptic transmission. Neuron *84*, 764–777. 10.1016/j.neuron.2014.09.030.

55. Kim, S.E., Coste, B., Chadha, A., Cook, B., and Patapoutian, A. (2012). The role of Drosophila Piezo in mechanical nociception. Nature *483*, 209–212. 10.1038/nature10801.

56. Song, Y., Li, D., Farrelly, O., Miles, L., Li, F., Kim, S.E., Lo, T.Y., Wang, F., Li, T., Thompson-Peer, K.L., et al. (2019). The Mechanosensitive Ion Channel Piezo

Inhibits Axon Regeneration. Neuron *102*, 373-389.e6. 10.1016/J.NEURON.2019.01.050.

57. Dill, K.A. (1997). Additivity principles in biochemistry. J Biol Chem *272*, 701–704. 10.1074/jbc.272.2.701.

58. Borst, P. (2020). The malate-aspartate shuttle (Borst cycle): How it started and developed into a major metabolic pathway. IUBMB Life *72*, 2241–2259. 10.1002/iub.2367.

59. Pezzulo, G., Zorzi, M., and Corbetta, M. (2021). The secret life of predictive brains: what's spontaneous activity for? Trends Cogn Sci *25*, 730–743. 10.1016/j.tics.2021.05.007.

60. Cadwell, C.R., Palasantza, A., Jiang, X., Berens, P., Deng, Q., Yilmaz, M., Reimer, J., Shen, S., Bethge, M., Tolias, K.F., et al. (2016). Electrophysiological, transcriptomic and morphologic profiling of single neurons using Patch-seq. Nat Biotechnol *34*, 199–203. 10.1038/nbt.3445.

61. Wong, C.-O., Karagas, N.E., Jung, J., Wang, Q., Rousseau, M.A., Chao, Y., Insolera, R., Soppina, P., Collins, C.A., Zhou, Y., et al. (2021). Regulation of longevity by depolarization-induced activation of PLC-β-IP3R signaling in neurons. Proc Natl Acad Sci U S A *118*. 10.1073/pnas.2004253118.

62. Brodersen, K., Gallusser, F., Koehler, J., and Remy, N. (2015). Inferring causal impact using Bayesian structural time-series models.

63. Giorgino, T. (2009). Computing and Visualizing Dynamic Time Warping Alignments in *R*□: The **dtw** Package. J Stat Softw *31*, 1–24. 10.18637/jss.v031.i07.

64. Galili, T. (2015). dendextend: an R package for visualizing, adjusting and comparing trees of hierarchical clustering. Bioinformatics *31*, 3718–3720. 10.1093/bioinformatics/btv428.

65. Abadi, M., Agarwal, A., Barham, P., Brevdo, E., Chen, Z., Citro, C., Corrado, G.S., Davis, A., Dean, J., Devin, M., et al. TensorFlow: Large-Scale Machine Learning on Heterogeneous Distributed Systems.

FIGURE LEGENDS

Figure 1. Temporally correlated changes in Laconic in response to glucose

(A) Representative images neurons dissociated from brains of *Drosophila* larvae expressing *UAS-Laconic* under the control of *d42-GAL4* glutamatergic/motor neuron driver (*d42>Laconic* neurons). Venus and mTFP intensities and mTFP/Venus ratio (Laconic ratio) are shown. Laconic ratio is equivalent to cytosolic [lactate].

(B) Traces showing normalized Laconic ratios in *d42>Laconic* neurons (n = 135 neurons). Arrow indicates time of 5 mM glucose application.

(C) Schematic showing differences between Euclidean time series matching and DTW. The longer sinusoid is a stretched version of the shorter sinusoid. While Euclidean matching determined correlations between values at the same absolute time values, DTW can stretch and compress the time series to ensure optimal correlation.

(D) Heatmap showing the hierarchical clustering of the Laconic ratios in *d42>Laconic* neurons. Arrow on the right indicates that all the ratios were from the time after the addition of 5 mM glucose. Axes corresponding to the time and individual cells are indicated. Ward's method on the distance matrix generated by DTW revealed the four indicated clusters.

(E) Traces showing normalized Laconic ratios in *d42>Laconic* neurons belonging to the indicated clusters. Responses of individual neurons are shown in grey. Colored lines represent mean ± SEM of the population responses. Arrows indicate time of 5 mM glucose application.

(F) Traces showing mean ± SEM of the Laconic ratios for each indicated cluster. Arrow indicates time of 5 mM glucose application.

(G) Bar-graph showing median ± 95% confidence intervals of the integrated changes in Laconic ratios in the indicated clusters.

(H) Traces showing the change in variance of the indicated neuronal populations over time. Arrow indicates time of 5 mM glucose application.

(I) Same as (D) but for the time points before the application of glucose. Arrow on the right represents the last point of time before the application of 5 mM glucose.

(J) Same as (E), but for clusters shown in (I).

Figure 2. Temporally correlated changes in Laconic ratios in response to the physical act of buffer application

(A) Traces showing normalized Laconic ratios in dissociated *d42>Laconic* neurons (n = 501 neurons). Arrow indicates time of buffer application.

(B) Heatmap showing the hierarchical clustering of the Laconic ratios in *d42>Laconic* neurons. Arrow on the right indicates that all the ratios were from the time after addition of the buffer. Axes correspond to time and individual cellular responses. Three clusters were determined by the use of Ward's clustering method on the distance matrix generated by DTW.

(C) Traces showing the change in variance of the indicated neuronal populations over time. Arrow indicates time of buffer application.

(D) Traces showing normalized Laconic ratios in *d42>Laconic* neurons belonging to the indicated clusters. Responses of individual neurons are shown in grey. Colored lines represent mean ± SEM of the population responses. Arrows indicate time of buffer application.

(E) Bar-graph showing median ± 95% confidence intervals of integrated changes in the Laconic ratios in the indicated clusters.

Figure 3. An autoencoder can compare and contrast the Laconic ratios evoked by application of glucose versus buffer alone

(A) Schematic showing the architecture of the autoencoder used. The activation functions used in each layer are indicated.

(B) Traces represent mean ± SEM of the population responses for each indicated cluster. Arrows indicate time of glucose or buffer application. Blue traces represent the ground truth and red traces represent the values reconstructed by the autoencoder. Bar-graph in bottom right shows mean ± SEM of the mean square error (MSE) associated with the reconstruction. All comparisons for statistical significance were made with the MSE associated with reconstruction of buffer cluster 1. ****, $P < 0.0001$ and n.s., not significant, Mann Whitney tests.

(C) Heat map showing the *P*-value matrix generated by the comparisons of clusters associated with application of glucose with those evoked by buffer alone. $P > 0.05$ for comparison of buffer cluster 1 and glucose cluster 2 indicate that these clusters have similar latent characteristics.

(D) Traces show mean ± SEM of the Laconic ratios for the indicated clusters. Arrow indicates the time of glucose or buffer application. Bar-graph show median ± 95% confidence intervals of integrated changes in the Laconic ratios in the indicated clusters. n.s., not significant, Mann Whitney tests.

(E) Traces show mean ± SEM of the Laconic ratios for the indicated clusters. Arrow indicates the time of glucose or buffer application. Bar-graph show median ± 95% confidence intervals of the integrated changes in the Laconic ratios in the indicated clusters.

Figure 4. Changes to Laconic ratios in response to metabolites that augment ATP production and drugs that inhibit ATP production

(A, B, D, E, G, H) Traces showing mean ± SEM of the Laconic ratios for the indicated clusters. Arrows indicate time of application. (Number of neurons: pyruvate treatment = 183; oligo A treatment = 145; 2DG treatment = 312).

(C, F, I) Bar graphs showing median ± 95% confidence intervals of integrated changes in the Laconic ratios in the indicated clusters. ****, $P < 0.0001$, ***, $P < 0.001$, n.s., not significant, Mann Whitney tests.

Figure 5. Assessment of the variability of Laconic responses

(A) Schematic showing the strategy used for calculating Shannon entropies for each cluster. Formula for Shannon entropy (H) is described in the box.

(B) Plots showing the ratios of the entropy in response to the indicated treatments relative to the entropy of buffer alone. Ground-truth values are represented by the blue lines. Boxes represent null datasets generated by shuffling response labels 1000 times. ***, $P < 0.001$, n.s., not significant, non-parametric bootstrap tests. NA indicates that entropy could not be calculated for 2DG because both P_{pos} and P_{neg} are zero for this treatment.

Figure 6. Evolution of low-dimensional projections of population responses

(A) 3D representations of the latent states of the indicated clusters evoked by the application of buffer alone. Each representation is rotated along the indicated axis by 90°. Colors represent evolution of time. Entropy associated with each cluster (H) is indicated on the right.

(B) Same as (A) but for clusters evoked by the application of 5 mM glucose.

(C) Same as (A) but for clusters evoked by the application of 1 mM pyruvate.

(D) Same as (A) but for clusters evoked by the application of 10 µM oligo A.

Figure 7. Pre-stimulus fluctuations in cytosolic [lactate] are predictive of post-stimulus responses

(A) Schematic showing the training and testing protocols for the deep-learning model designed to predict post-response labels on the basis of pre-response Laconic traces.

(B) Bar-graph in which the blue bars represent accuracy with which the model predicted test labels during 5-fold cross validation. Bars in magenta represent accuracy after training the model with the dataset in which response labels were scrambled. Relevant treatments are indicated below the graph. Since the folds are generated randomly, we performed these analyses 300 times for each treatment. Values shown represent mean ± SEM for the accuracies determined by these repetitions. Dots represent individual values. ****, $P < 0.0001$, Mann Whitney tests.

(C) Bar-graph showing the difference in prediction accuracies for the training and test datasets. The mean reduction in accuracies for all treatments are <5%, which argues

against overfitting. Values shown represent mean ± SEM for the differences determined by the 300 repetitions described in (B).

(D) Schematic showing the training and testing protocols for the deep-learning model designed to predict Laconic traces post-response on the basis of pre-response Laconic traces.

(E) Traces showing mean values of the post-response Laconic ratios for the ground-truth (blue) and predicted values (red). Data were from responses to the application of buffer alone. Test and training sets were the same for the data in this panel.

(F) Traces showing mean values of the post-response Laconic ratios for the ground-truth (green), predicted values (purple), and predicted values when model was trained on scrambled post-response values (orange). Data shown were from responses to the application of buffer alone. For the data shown in this panel, the test and training sets were distinct.

(G) Bar-graph showing the mean square error (MSE) associated with the prediction in the indicated datasets and in response to the indicated treatments. Values shown represent mean ± SEM for the MSEs determined during the 5-fold cross validation. ***, $P < 0.001$; **, $P < 0.01$; n.s., not significant, Mann Whitney tests.

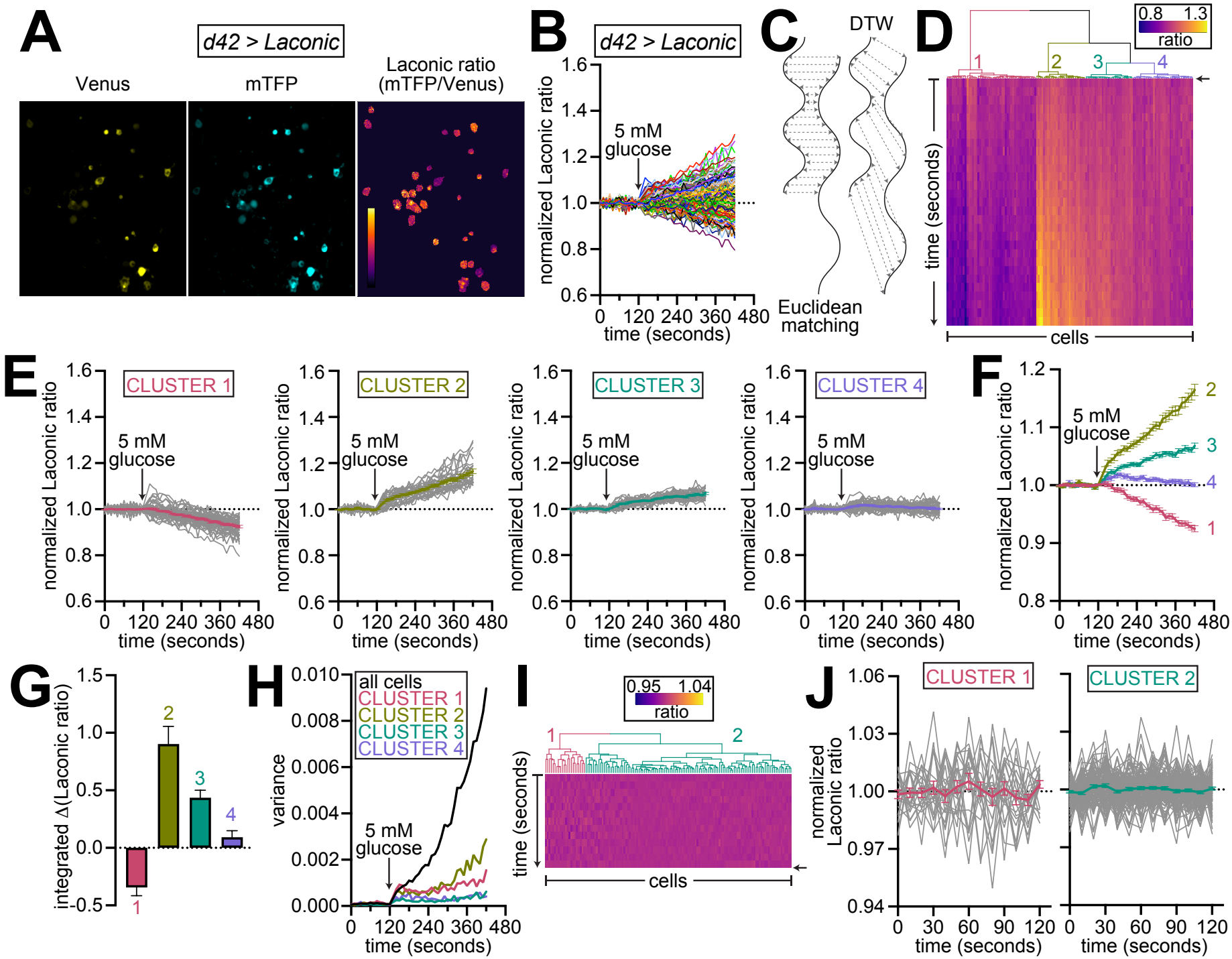
A
d42 > Laconic
Venus
mTFP
Laconic ratio (mTFP/Venus)
B
d42 > Laconic
normalized Laconic ratio
5 mM glucose
time (seconds)
C
DTW
Euclidean matching
D
0.8 1.3
ratio
time (seconds)
cells
E
CLUSTER 1
CLUSTER 2
CLUSTER 3
CLUSTER 4
normalized Laconic ratio
5 mM glucose
time (seconds)
F
normalized Laconic ratio
5 mM glucose
time (seconds)
G
integrated Δ(Laconic ratio)
H
all cells
CLUSTER 1
CLUSTER 2
CLUSTER 3
CLUSTER 4
variance
5 mM glucose
time (seconds)
I
0.95 1.04
ratio
time (seconds)
cells
J
CLUSTER 1
CLUSTER 2
normalized Laconic ratio
time (seconds)

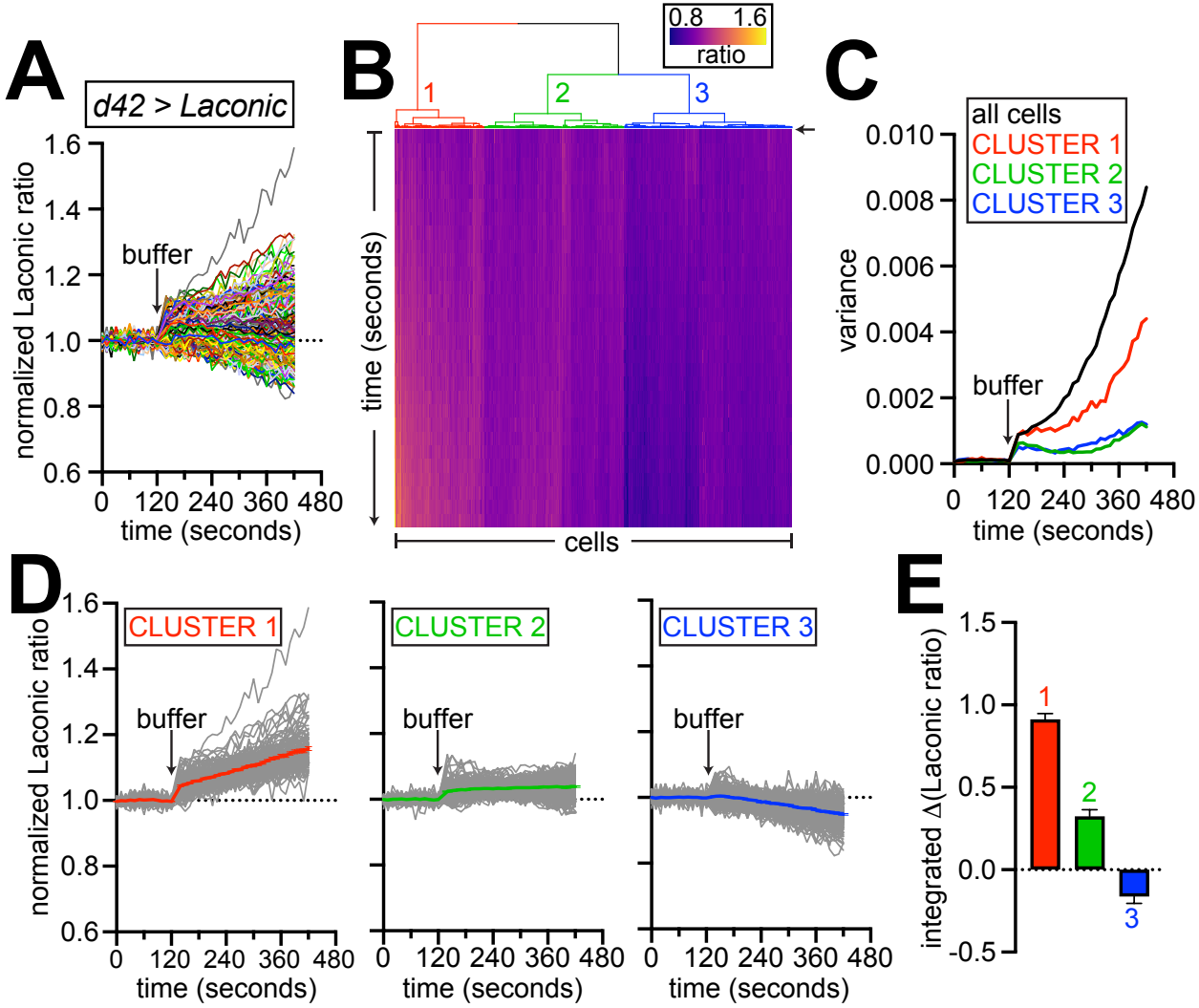
A
d42 > Laconic
normalized Laconic ratio
1.6
1.4
1.2
1.0
0.8
0.6
buffer
0 120 240 360 480
time (seconds)
B
0.8 1.6
ratio
1
2
3
time (seconds)
cells
C
all cells
CLUSTER 1
CLUSTER 2
CLUSTER 3
variance
0.010
0.008
0.006
0.004
0.002
0.000
buffer
0 120 240 360 480
time (seconds)
D
CLUSTER 1
CLUSTER 2
CLUSTER 3
normalized Laconic ratio
buffer
0 120 240 360 480
time (seconds)
E
integrated Δ(Laconic ratio)
1.5
1.0
0.5
0.0
-0.5
1
2
3

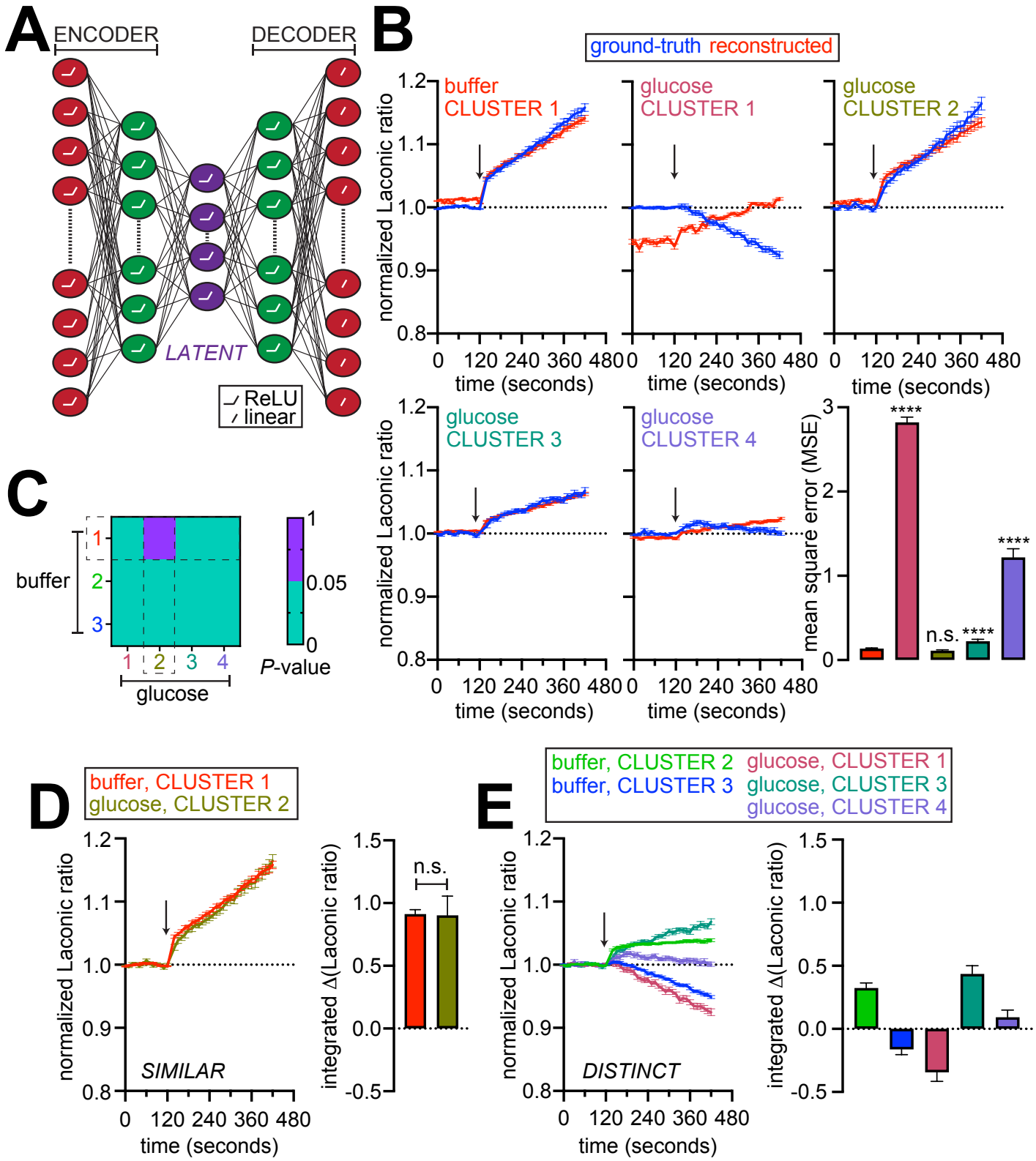
A
ENCODER
DECODER
LATENT
ReLU
linear
B
ground-truth reconstructed
buffer
CLUSTER 1
glucose
CLUSTER 1
glucose
CLUSTER 2
glucose
CLUSTER 3
glucose
CLUSTER 4
normalized Laconic ratio
time (seconds)
mean square error (MSE)
****
n.s.
C
buffer
glucose
P-value
D
buffer, CLUSTER 1
glucose, CLUSTER 2
SIMILAR
integrated Δ(Laconic ratio)
n.s.
E
buffer, CLUSTER 2
buffer, CLUSTER 3
glucose, CLUSTER 1
glucose, CLUSTER 3
glucose, CLUSTER 4
DISTINCT

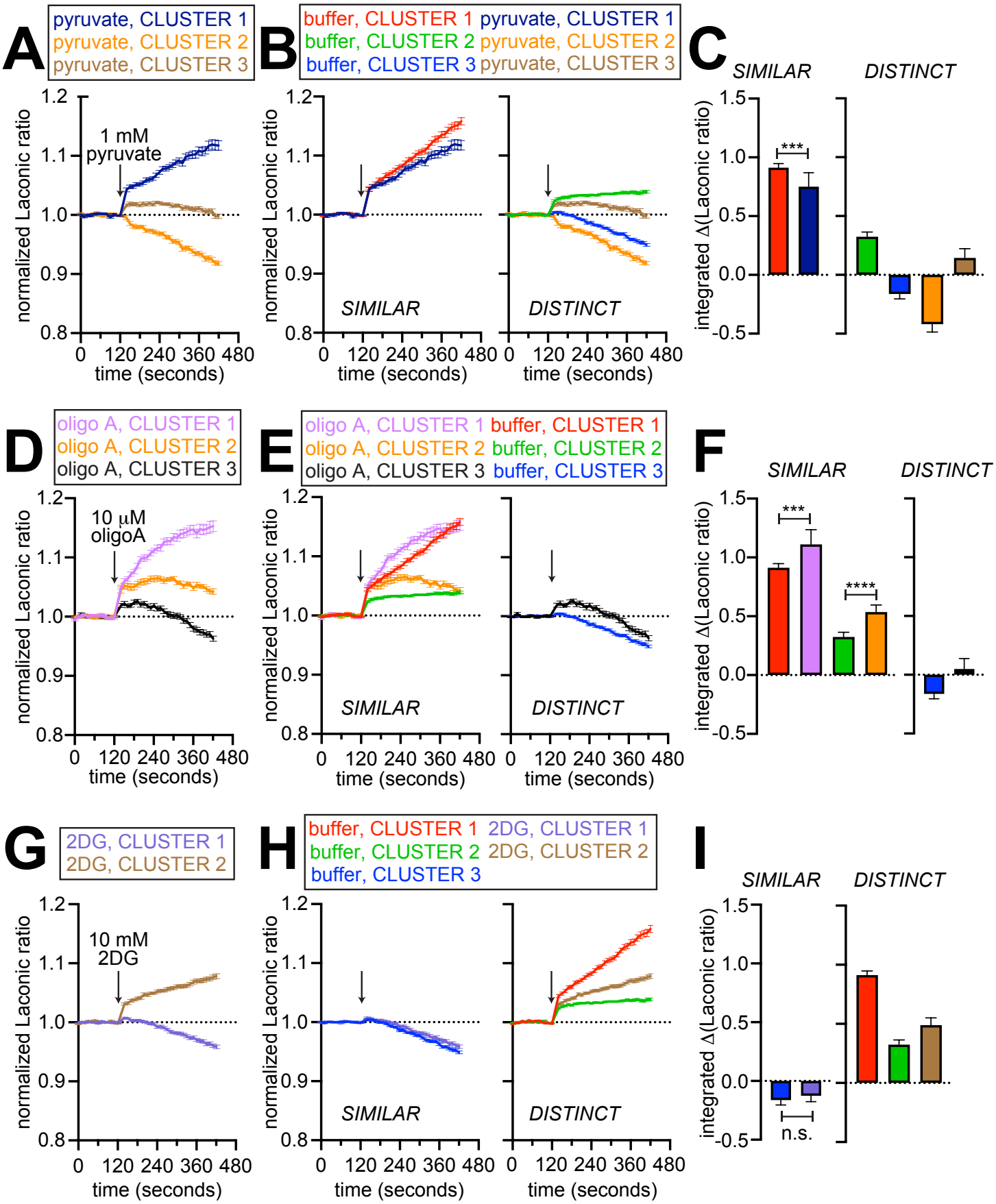
A
pyruvate, CLUSTER 1
pyruvate, CLUSTER 2
pyruvate, CLUSTER 3
1 mM pyruvate
normalized Laconic ratio
time (seconds)
B
buffer, CLUSTER 1
buffer, CLUSTER 2
buffer, CLUSTER 3
pyruvate, CLUSTER 1
pyruvate, CLUSTER 2
pyruvate, CLUSTER 3
SIMILAR
DISTINCT
C
SIMILAR
DISTINCT
integrated Δ(Laconic ratio)
***
D
oligo A, CLUSTER 1
oligo A, CLUSTER 2
oligo A, CLUSTER 3
10 μM oligoA
E
oligo A, CLUSTER 1
oligo A, CLUSTER 2
oligo A, CLUSTER 3
buffer, CLUSTER 1
buffer, CLUSTER 2
buffer, CLUSTER 3
F
***
****
G
2DG, CLUSTER 1
2DG, CLUSTER 2
10 mM 2DG
H
buffer, CLUSTER 1
buffer, CLUSTER 2
buffer, CLUSTER 3
2DG, CLUSTER 1
2DG, CLUSTER 2
I
n.s.

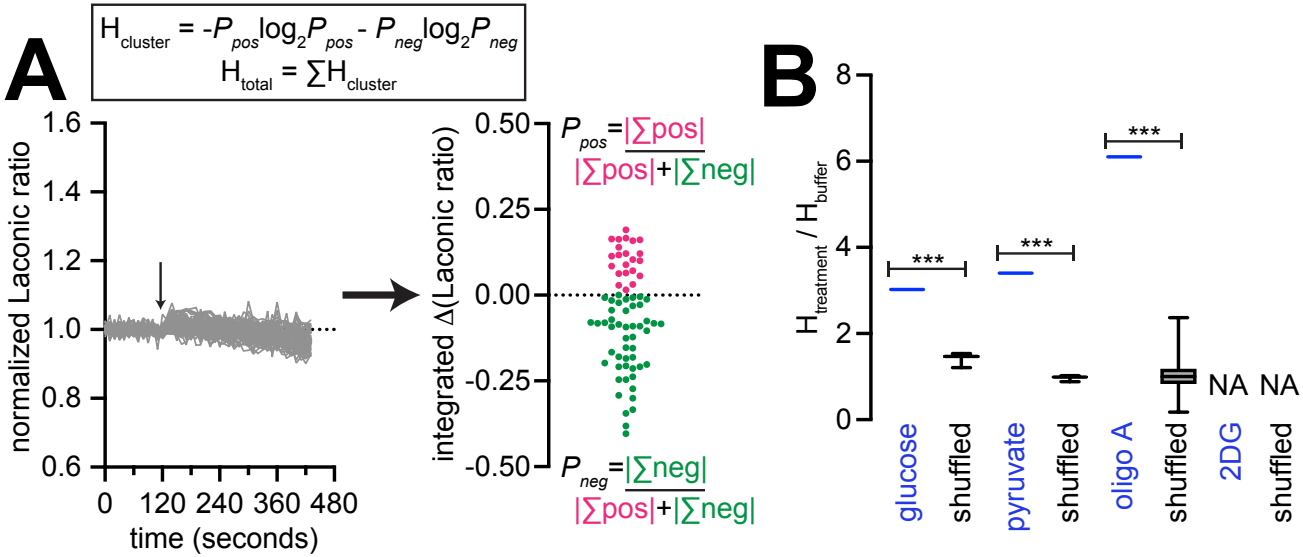
A
$H_{cluster} = -P_{pos}\log_2 P_{pos} - P_{neg}\log_2 P_{neg}$
$H_{total} = \sum H_{cluster}$
normalized Laconic ratio
1.6
1.4
1.2
1.0
0.8
0.6
0
120
240
360
480
time (seconds)
integrated Δ(Laconic ratio)
0.50
0.25
0.00
-0.25
-0.50
$P_{pos} = \frac{|\sum pos|}{|\sum pos| + |\sum neg|}$
$P_{neg} = \frac{|\sum neg|}{|\sum pos| + |\sum neg|}$
B
$H_{treatment} / H_{buffer}$
8
6
4
2
0
***
***
***
NA
NA
glucose
shuffled
pyruvate
shuffled
oligo A
shuffled
2DG
shuffled

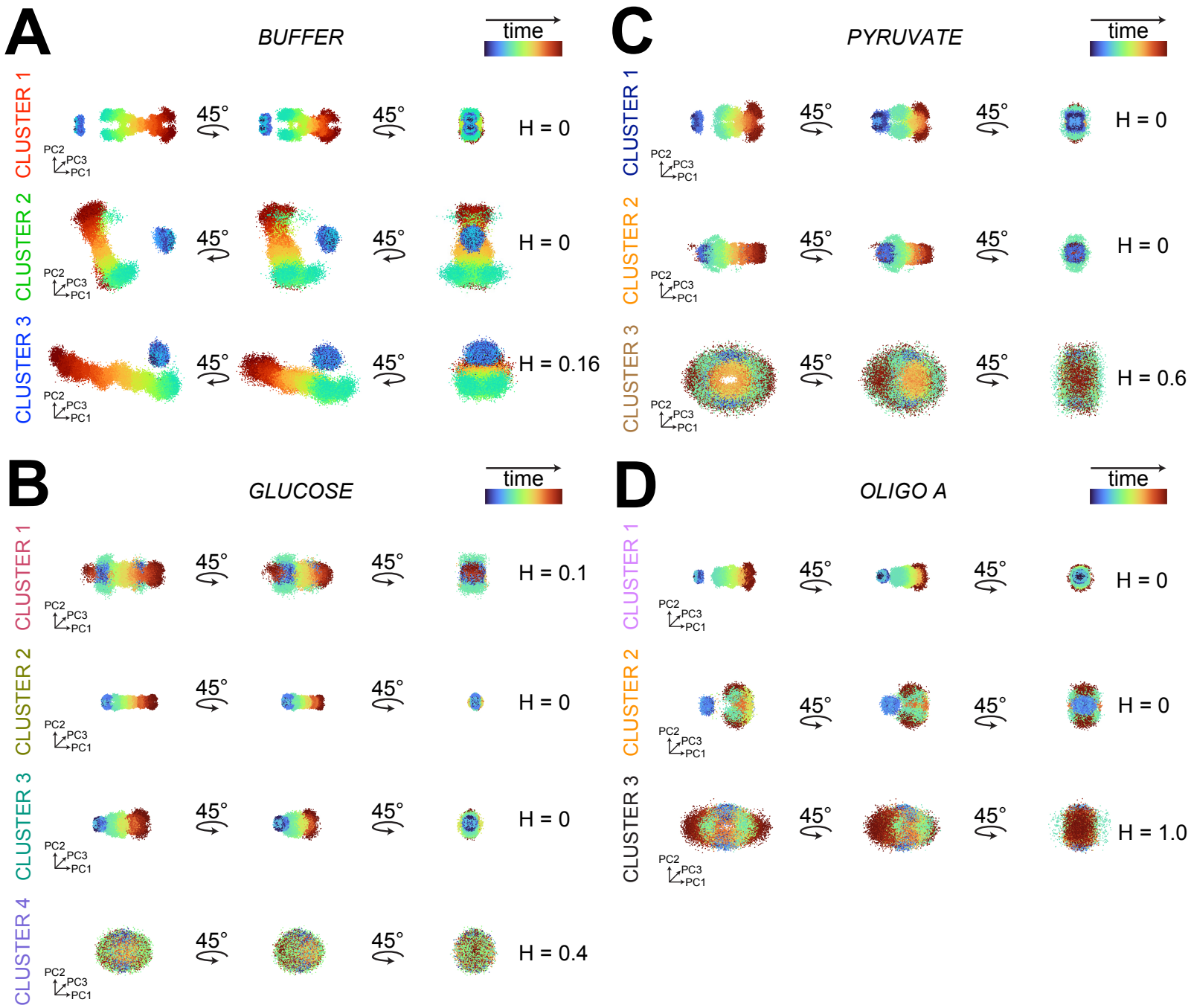
A
BUFFER
time
CLUSTER 1
CLUSTER 2
CLUSTER 3
PC2
PC3
PC1
45°
H = 0
H = 0
H = 0.16
B
GLUCOSE
time
CLUSTER 1
CLUSTER 2
CLUSTER 3
CLUSTER 4
H = 0.1
H = 0
H = 0
H = 0.4
C
PYRUVATE
time
CLUSTER 1
CLUSTER 2
CLUSTER 3
H = 0
H = 0
H = 0.6
D
OLIGO A
time
CLUSTER 1
CLUSTER 2
CLUSTER 3
H = 0
H = 0
H = 1.0

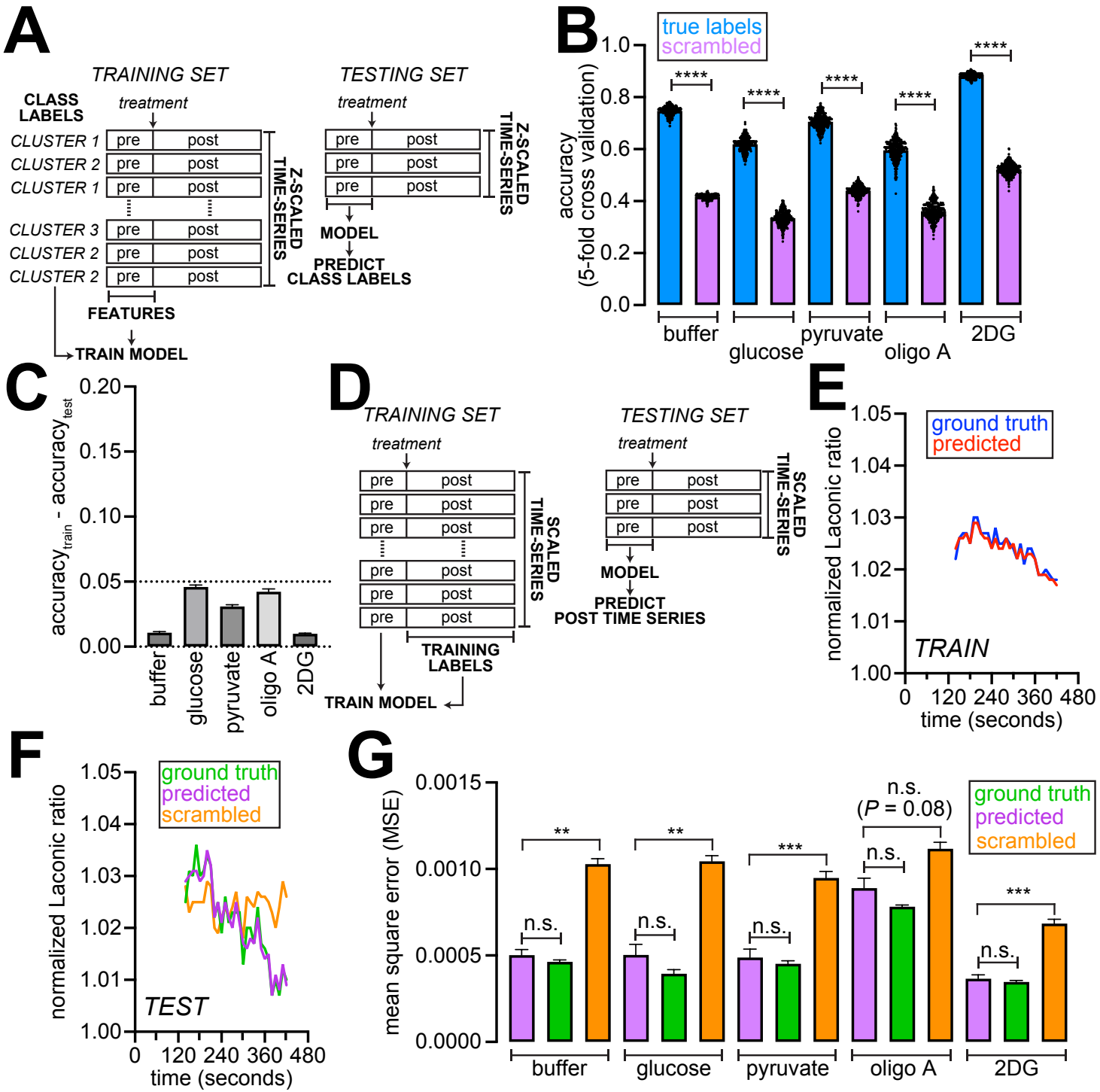
A
TRAINING SET
CLASS LABELS
treatment
CLUSTER 1
CLUSTER 2
CLUSTER 1
CLUSTER 3
CLUSTER 2
CLUSTER 2
pre
post
Z-SCALED TIME-SERIES
FEATURES
TRAIN MODEL
TESTING SET
treatment
MODEL
PREDICT CLASS LABELS
B
true labels
scrambled
accuracy (5-fold cross validation)
1.0
0.8
0.6
0.4
0.2
0.0
****
buffer
glucose
pyruvate
oligo A
2DG
C
accuracy_test - accuracy_train
0.20
0.15
0.10
0.05
0.00
buffer
glucose
pyruvate
oligo A
2DG
D
TRAINING SET
treatment
pre
post
SCALED TIME-SERIES
TRAINING LABELS
TRAIN MODEL
TESTING SET
treatment
MODEL
PREDICT POST TIME SERIES
E
ground truth
predicted
normalized Laconic ratio
1.05
1.04
1.03
1.02
1.01
1.00
TRAIN
0
120
240
360
480
time (seconds)
F
ground truth
predicted
scrambled
normalized Laconic ratio
1.05
1.04
1.03
1.02
1.01
1.00
TEST
0
120
240
360
480
time (seconds)
G
mean square error (MSE)
0.0015
0.0010
0.0005
0.0000
n.s.
**
***
n.s. (P = 0.08)
ground truth
predicted
scrambled
buffer
glucose
pyruvate
oligo A
2DG